Progress in Additive Manufacturing
https://doi.org/10.1007/s40964-024-00785-9

FULL RESEARCH ARTICLE

Reactive formation of C_3N_4 as a by-product of AISI 1070 parts produced by laser powder bed fusion in N_2 atmosphere

Andrea Gatto[1] · Emanuele Tognoli[1] · Riccardo Groppo[2] · Marcello Cabibbo[3] · Maria Laura Gatto[3] · Simona Sabbatini[4] · Paolo Mengucci[4]

Received: 6 May 2024 / Accepted: 28 August 2024

Abstract
In metal additive manufacturing (AM), inert gases are traditionally used to achieve a controlled atmosphere and mitigate the effects of residual reactive gases. However, the interaction between gases and laser processes, particularly in reactive laser powder bed fusion (RL-PBF) technology, offers the possibility of opening up new avenues for material synthesis. In this experimental work, the authors observed the presence of C_3N_4 in the residual powder during the manufacture of AISI 1070 steel parts by L-PBF, indicating a reactive process occurred during parts production. This investigation revealed the formation in the working chamber of a waste product containing C_3N_4 carbon nitride, due to the reaction between the carbon released from the steel and the nitrogen in the chamber. Remarkably, despite carbon depletion, the final product of AISI 1070 steel complies with the specifications of use. Hence, the L-PBF machine was modified to allow black powder sampling from various locations in the chamber. Authors attempted to enhance the production of the C_3N_4 material by increasing the SED up to 7143 J/mm^2 to sublimate a pure graphite rod and concurrently manufacture parts in AISI 1070, in a nitrogen atmosphere. The results obtained at higher SED values showed that in both cases (graphite rod or AISI 1070 steel) a C_3N_4 compound in the black powder is formed in the investigated atmosphere by reaction of nitrogen atoms with the carbon atoms vaporized by the laser beam. Thus, the study highlights the novel achievement of synthesizing carbon nitride as a high-value by-product while producing functional AISI 1070 steel parts via L-PBF through reaction with nitrogen atmosphere.

Keywords Additive manufacturing · Reactive laser powder bed fusion · Nitrogen atmosphere · Carbon nitride · Filtering system

1 Introduction

In the additive manufacturing (AM) of metals, inert gases such as nitrogen and argon are generally used to ensure a controlled atmosphere and mitigate the effects of residual reactive gases (especially oxygen). However, the synergistic interaction between gases and laser processes sets novel possibilities for manipulating material composition and phase formation by reactive laser powder bed fusion (RL-PBF) technology [1].

Since RL-PBF leads to the formation of carbide- and nitride-based phases and thus extends the design flexibility of multi-material components, several applications have been explored in the literature recently. For instance, localized surface modifications can be obtained directly through the RL-PBF production process at specific sites on the printed component. This approach bypasses the ex situ deposition methods, which are effective in creating ceramic layers but suffer from certain drawbacks, such as the inability to process complex surfaces and reentrant shapes, and thermal modifications in the substrate material [2]. According to Sahasrabudhe et al. [2], composite coatings of titanium nitrides and calcium titanate on an α-Ti

✉ Maria Laura Gatto
m.l.gatto@univpm.it

[1] Dipartimento di Ingegneria "Enzo Ferrari", Università di Modena e Reggio Emilia, Via Vivarelli 10, 41125 Modena, Italy

[2] 3D4MEC S.r.l, Via Porrettana 48, 40037 Sasso Marconi, BO, Italy

[3] Dipartimento DIISM, Università Politecnica delle Marche, via Brecce Bianche 12, 60131 Ancona, Italy

[4] Dipartimento SIMAU, Università Politecnica delle Marche and UdR INSTM, via Brecce Bianche 12, 60131 Ancona, Italy

Published online: 09 September 2024

matrix were generated in situ by reactive multi-material laser engineered net shaping (LENS™), where a mixture of Ti-6Al-4 V powder and calcium phosphate (CaP) was processed in an oxygen-free, nitrogen-argon environment.

In addition to surface treatment directly during the AM process, bulk composites were also investigated. The in-situ formation of metallic glass–ceramic composites was explored by Goetz et al. [1] as a possibility for AM processing. The formation of ZrN in a Zr-based bulk metallic glass is observed after processing using RL-PBF [1], the results were subordinate to the gas solubility in the melting pool, the phase diagram and the process conditions. Furthermore, the reactive AM approach paves the way for in situ strengthening of pure metals and alloys. According to Dong et al. [3], strong and ductile pure Ti was synthesized via an approach involving ball-milled pure Ti powder and RL-PBF in an Ar-N_2 atmosphere. RL-PBF has also been shown to enable the in-situ synthesis of carbide and nitride ceramic phases such as Cr_3C_2 and CrN, overcoming previous limitations in the additive manufacturing of non-oxide materials [4]. The reactive approach may as well be viable for the additive manufacturing of numerous ultra-high-temperature ceramic materials (HfC, ZrC, TiC, HfN, ZrN, and TiN), that cannot be readily produced using current methods [5].

The use of reactive atmosphere for stainless steel is widespread and the main goal is to obtain oxide dispersion-strengthened steels (ODS) in a non-conventional way. The main advantages are the possibility of obtaining customizable products by a cost-effective process. The main authors who have worked in this field are Haines et al. [6]; Wang et al. [7]; Yin et al. [8] and Horn et al. [9]. Each author has applied the L-PBF technology with different reactive atmospheres and with different process parameters, which are listed in Table 1.

All authors agree that the use of a reactive atmosphere, either carbon dioxide or oxygen, makes it possible to obtain oxides in the final products, in nano- or micron size. Oxygen tends to combine with yttrium, and when it is not available, the preferred oxygen getter is aluminium. Yin et al. investigated the difference in end products that results from using different oxygen getters at different atmospheres. His studies emphasize that yttrium produces the smallest oxide diameter (approx. 50 nm in all atmospheres) and the highest oxygen percentage (approx. 600 ppm) where a plateau is reached. Under these conditions, an acceptable amount of ODS is obtained, comparable to other commercial counterparts and sufficient to enhance mechanical properties, but it is not possible to obtain a high-density dispersion of nano-oxides due to surface oxidation and oxide agglomeration.

Despite the various applications of reactive additive fabrication witnessed in the most recent literature, no study has yet investigated its benefits in the production of new materials as a by-product of the RL-PBF production process in N_2 atmosphere.

The present experimental study originated from the detection of C_3N_4 in the residual powder remaining in the working chamber after the production of AISI 1070 steel parts by laser powder bed fusion (L-PBF) in a nitrogen atmosphere. Findings suggested a reactive process involving carbon atoms vaporized from the metal and the N_2 gas. To collect the carbon nitride formed, the L-PBF machine was modified so that the black powder could be sampled from various points in the chamber. The black powder consists of the waste products formed in the build chamber during the production process. Black powder is blown out of the

Table 1 Use of L-PBF technology in literature with different reactive atmospheres and process parameters to obtain oxide dispersion-strengthened steels

Work	Powder	Atmosphere	Power (W)	Scanning speed (mm/s)	Layer thickness (µm)	Hatch distance (µm)
Haines et al. [6]	Fe—19.2 Cr—4.59 Al—0.55 Ti—0.0262 —0.0055C	100% Ar 0.02% O_2-Ar 2% CO_2-Ar 8% CO_2-Ar 100% CO_2	140 170 200	600 1000 1400	30	90
Wang et al. [7]	Fe—22 Cr—5.1 Al—0.5 Ti—0.26 Y—0.0202 O—0.0686N	0.3% O_2-Ar 0.5% O_2-Ar 1% O_2-Ar 99.99% N_2	300	1318	30	110
Yin et al. [8]	316-L Si; 316-L Al; 316-L 0.5Y; 316-L 1.2Y; 316-L 2.0Y;	100% Ar 1% O_2-Ar 2% O_2-Ar	90	400 600 1000	25	80
Horn et al. [9]	Fe—14.99 Cr—0.15 Y—0.10 Ti—0.06O, this powder was gas atomized in Ar then in O_2	1% O_2-Ar 5% O_2-Ar Air	90	1500	20	80

building platform by the gas flow and then collected in the filtering system.

Carbon nitride organic materials are a versatile group of functional materials with significant potential for various applications in the field of energy and sustainability. Carbon nitrides, which are characterized by a high nitrogen-to-carbon ratio, are synthesized by thermal condensation of carbon with nitrogen-containing precursors. The special properties of carbon nitrides, such as tunable optical properties, high stability, biocompatibility and low cost, have stimulated interest in their applications in different fields [10]. The first synthesis of a polymeric carbon nitride was reported by Berzelius and Liebig in 1834 [11], making it one of the oldest synthesized polymers. Carbon nitrides exist in several allotropes with diverse properties, but the graphitic phase g-C_3N_4 is regarded as the most stable under ambient conditions, especially as a photocatalyst for hydrogen production by water splitting [12, 13]. Moreover, g-C_3N_4 has demonstrated high thermal, mechanical, and chemical stability due to its structure based on the tri-s-triazine (C_6N_7) building blocks and strong covalent bonds between carbon and nitrogen atoms, as well as suitable optoelectronic properties due to its band gap value $E_g = 2.7$ eV [14, 15]. Nanoscale graphitic carbon nitride has been synthesized in the form of three-dimensional (3D) nanoparticles, two-dimensional (2D) nanosheets and one-dimensional (1D) chains [16–18]. Nevertheless, the performance of C_3N_4 in photocatalytic applications is still limited since it strongly depends on the crystal structure, porosity, charge transport, and limited light harvesting in the visible and near-infrared regions. For this reason, crystalline carbon nitrides with a different stoichiometry than C_3N_4 have recently emerged, exhibiting very promising properties for optoelectronic applications [19]. Generally, C_xN_y materials are synthesized by organic modifications, oxidation treatments, inorganic doping, and mechanical denaturation [10]. Many of the investigated production technologies use hazardous and non-environmentally friendly components. Other solutions (e.g. polymer templates) are not robust enough for large scale production.

The findings from three key experiments are presented in this paper. First, the authors report on the successful manufacturing of AISI 1070 parts by L-PBF with optimized process parameters and the simultaneous reactive formation of C_3N_4 as a by-product. In this case, values of the surface energy density (SED) in the range of 0.67–15 J/mm^2 were explored. Secondly, a rod of pure graphite was exposed to the laser beam by increasing the SED up to 7143 J/mm^2, to cause the sublimation of the graphite and thus the reaction of the carbon atoms with the nitrogen atmosphere, for enhancing the production of the C_3N_4 compound. Thirdly, the authors attempted to improve the production of the C_3N_4 material at high values of SED as the second experiment, to manufacture parts in AISI 1070 in a nitrogen atmosphere. The results obtained at higher SED values showed that in both cases (graphite rod or AISI 1070 steel) a C_3N_4 compound is formed in the investigated atmosphere by reaction of nitrogen atoms with the carbon atoms vaporized by the laser beam. XRD and FTIR analyses of the black powder collected in the filtering system of the L-PBF machine evidenced a higher efficiency of C_3N_4 formation in the case of sublimation of the pure graphite rod, than in the L-PBF of AISI 1070 steel. These results pave the way for the investigation and optimization of new methods for the production of C_3N_4 materials by reactive laser powder bed fusion (RL-PBF).

2 Experimental procedure

2.1 Manufacturing of AISI 1070 steel specimens by L-PBF

AISI 1070 steel gas-atomized powder in the diameter range 15–53 µm was supplied by MIMETE Srl. The chemical composition of the standard AISI 1070 is listed in Table 2, based on the manufacturer's specifications.

To optimize the process parameters for AISI 1070, three cubes of $12 \times 12 \times 12$ mm^3 were fabricated for each process parameters combination reported in Table 3 using a 3D4Steel Laser Powder Bed Fusion (L-PBF) manufacturing system (3D4MEC Srl, Sasso Marconi (BO), Italy). The machine used a 1000 W Yb-fiber laser operating in a nitrogen atmosphere, provided by an on-board local generator. An oxygen probe ensured that the oxygen content in the chamber remained below 0.2% throughout the entire manufacturing process. The cubes were fabricated atop a support structure on a steel baseplate of 110×110 mm^2, employing a standard raster scanning strategy with an 80° rotation between layers. In addition to raster scanning, pre-contour and post-contour passes were executed along the outer edge of each slice.

Table 2 Chemical composition of the raw powder as provided by Mimete Srl according to AISI 1070 standard. Element concentration in wt.%

C	Mn	Cr	Ni	Si	Mo*	P*	S*
0.65–0.73	0.6–0.9	0.2–0.6	0.2–0.6	0.15–0.35	0.1	0.03	0.03

* %max

Table 3 Process parameters used for the optimization of AISI 1070 L-PBF process; Power (P), scanning speed (v), hatching space (h), layer thickness (t) and surface energy density (SED)

Sample name	P (W)	v (mm/s)	h (mm)	t (mm)	SED [J/mm^2]
P170v1400	170	1400	0.14	0.05	0.87
P170v1600		1600			0.76
P170v1800		1800			0.67
P190v150	190	150			9.05
P190v1400		1400			0.97
P190v1600		1600			0.85
P190v1800		1800			0.75
P210v100	210	100			15.00
P210v150		150			10.00
P210v200		200			7.50
P210v1600		1600			0.94
P210v1800		1800			0.83

To correlate the density of the obtained specimens and the deposition parameters, surface energy density (SED) was calculated by Eq. (1):

$$\mathrm{SED} = \frac{P}{vh} \tag{1}$$

where P is the power of the laser beam, v the scanning speed and h the hatch distance.

Several papers in literature proposed correlating parameters, such as laser power, scanning speed and hatching space, using an approach based on energy density, which was demonstrated to control the material density and pore distribution [20, 21]. According to Gordon et al. [22], a full density sample can be obtained within the "process window" by optimizing printing parameters, generally power (P) and scanning speed (v).

Two SED regimes were adopted: (a) high surface specific energy (SED > 7 J/mm^2) and (b) low surface specific energy (SED < 1 J/mm^2).

The density of the samples was measured using the Archimedes technique according to ASTM B962-17. For each AISI 1070 L-PBF process condition with a high surface specific energy (SED > 7 J/mm^2), the density was measured on three samples, and results were presented as the average value.

During the processing of AISI 1070, the unmelted residual powder in the chamber after production was analyzed. In a second stage of the research, the 3D4Steel L-PBF manufacturing system was modified to allow different sampling points for black powder. Figure 1 shows the sampling points introduced with the 3D4Steel machine modification (marked with asterisks in Fig. 1). Additionally, previous experiences indicate that the use of high surface energy densities necessitates a complex optimization

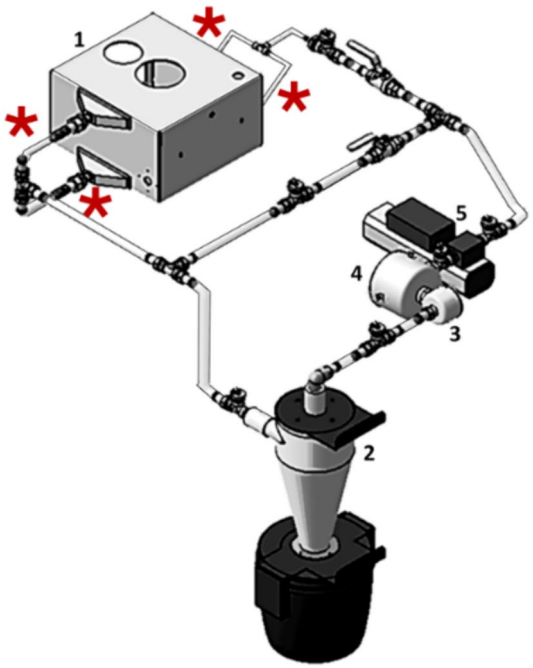

Fig. 1 Closed loop gas flow scheme: (1) working chamber; (2) cyclone; (3) rough filter; (4) fine filter; (5) pump. Asterisks indicate the black powder sampling points

phase of the protective gas circuit. Therefore, the 3D4Steel L-PBF machine underwent a partial modification to assess the pressure losses upstream and downstream of each device in the gas circuit, including the pressure drop across the cyclone filter, pre-filter, final filter, as well as the inlet and outlet of the work chamber.

2.2 Structural characterization by SEM, XRD and FTIR

The chemical composition, microstructure and morphology of the AISI 1070 raw powder and specimens produced with a SED in the range of 0.67–15 J/mm^2 were investigated using a Tescan Vega3 scanning electron microscope (SEM) equipped with an EDAX microanalysis (EDS) system. A Bruker D8 Advance X-ray diffractometer operating at $V = 40$ kV and $I = 40$ mA with Cu Kα radiation in the angular range $2\theta = 20°$–$80°$ was used for the structural characterization of raw powder, residual powder, black powder and samples by X-ray diffraction (XRD). The XRD patterns were analyzed using the DIFFRAC.EVA software package including ICDD–PDF 2 for search/match analysis. The shape analysis of the XRD peaks was carried out using the OriginPro software package. The microstructure of the AISI 1070 sample was observed with an optical microscope (OM) after metallographic preparation and etching with 2% Nital.

The chemical analysis of the sample with maximum density was performed by Optical Emission Spectrometry (OES) (mass fraction) using a SPECTRO MAXX7 S Quantometer.

Fourier transform infrared spectroscopy (FTIR) was used to characterize the molecular structure of materials and investigate their degree of polymerization. In this analytical technique, infrared radiation is passed through the sample and the amount of radiation absorbed at different wavelengths is recorded. The resulting spectrum provides information about the chemical bonds and functional groups present in the material. Black powders formed during the sublimation of the graphite rod and the manufacturing of AISI 1070 parts at SED values up to 7143 J/mm^2 were characterized by FTIR. IR spectra were recorded in reflectance mode using a Perkin Elmer Spectrum GX1 spectrometer with the ATR accessory and a ZnSe crystal. The spectra were collected in the 4000–500 cm^{-1} range with a resolution of 4 cm^{-1}. Each spectrum was the average of 32 scans. The samples were placed directly on the ZnSe crystal without any preparation. Three IR spectra were recorded for each sample and the average absorbance spectrum was calculated. The background spectrum was obtained from the clean crystal before each measurement. The raw IR spectra were then converted to absorbance mode and vector normalized using Perkin-Elmer's Spectrum 10.4.0 software.

3 Results and discussion

3.1 *Production of AISI 1070 parts with optimized parameters and reactive formation of the C_3N_4 as a by-product*

SEM observations of the AISI 1070 raw powder revealed particles with numerous satellites (Fig. 2A), which compromise the sphericity and thus the smoothness of the powder itself. This condition could affect the uniformity and apparent density obtained by recoating and thus the dimensional tolerance and final density of the manufactured parts. The XRD investigation of the AISI 1070 raw powder is reported in Fig. 2B, showing that the powder consists entirely of α-Fe (ferrite), cubic (bcc), with the nominal lattice parameter $a = 0.28664$ nm (ICDD PDF file n. 06–0696). The estimation of the peak intensity by shape analysis of the XRD peaks visible in Fig. 2B evidenced a low preferential growth of the (101) crystallographic planes of the ferrite.

The optimum conditions for laser irradiation of high-density carbon steel depend on the carbon content in the steel powders [23]. According to Nakamoto et al. [23], the energy required for full densification decreases with increasing carbon content. This phenomenon can be attributed to the increased wettability of the molten Fe–C alloys resulting from higher carbon contents.

AISI 1070 specimens produced by L-PBF with low SED values (< 1 J/mm^2) exhibited surface porosity that made them unsuitable for the production of parts due to potential crack initiation sites. Minimization of process-induced porosity is the principal objective in additive manufacturing technology and a number of papers in literature have developed such topic. Therefore, only the relative density of the specimens produced with high SED values (> 7 J/

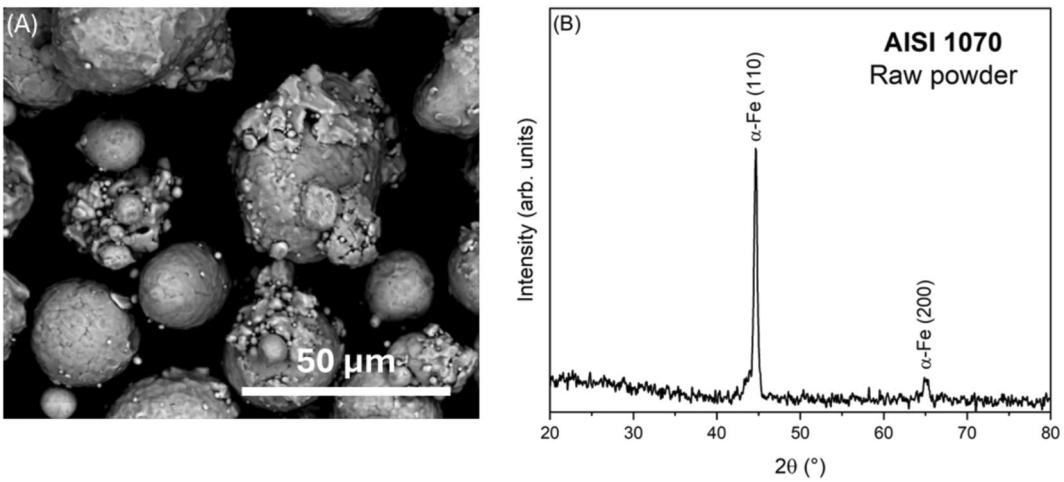

Fig. 2 Raw powder of AISI 1070: **A** SEM image and **B** XRD pattern

mm^2) was measured (Table 4). At each layer, the laser melts a depth of material corresponding to a multiple of the single layer thickness. The number of layers melted depends on the SED and is typically between four and six for our samples, ensuring material continuity through the sequence of layers. Table 4 reports the relative density of the samples at high SED values. At SED values ≥ 9 J/mm^2, all samples had a relative density $\rho \geq 98.6\%$, indicating near-full density according to Yue et al. [24].

AISI 1070 steel samples fabricated by L-PBF with the process parameters resulting in SED values listed in Table 4 have an overall porosity of about 1%. This is a significantly lower value compared to components produced by casting, for example, and therefore, meets the requirements of many applications. The chemical composition, microstructure and phase analysis were studied exclusively on the sample with the highest relative density, i.e. P210v100, which was produced with the highest SED value of 15 J/mm^2.

The experimental chemical composition of P210v100 measured by OES revealed a significant reduction in carbon content with respect to the raw powder, while other elements remained within the range of standard acceptance, as detailed in Table 5. The results of EDS are consistent with those of OES. Despite the notable disparity in composition between the AISI 1070 powder reported in Table 2 and the samples obtained by L-PBF (Table 5), mechanical properties (reserved data) of AISI 1070 produced samples are suitable for the end user applications.

The SEM micrograph in Fig. 3 illustrates the microstructure of the P210v100 specimen, after chemical etching. The microstructure is very similar to the microstructure of a normalised steel with the same composition described in the literature [25].

In addition to the AISI 1070 raw powder, the L-PBF P210v100 cubic sample and the unmelted powder left in the chamber after production (residual powder) were subjected to XRD investigations. All the results of the XRD analysis are shown in Fig. 4, with the patterns shifted vertically for better comparability. The patterns of the raw powder and the P210v100 sample are identical, indicating that they consist exclusively of α-Fe (ferrite), as shown in Fig. 4 (XRD patterns #1 and #2). On the contrary, the residual powder (XRD pattern #3 in Fig. 4) shows broad and low intensity peaks of C_3N_4, hexagonal, with nominal lattice parameters $a = 0.64978$ nm and $c = 0.46909$ nm (ICDD PDF file n. 53–0671), in addition to α-Fe.

The presence of C_3N_4 in the residual powder after the production of the AISI 1070 cube samples (Fig. 4) indicates a reactive process occurring in atmosphere inside the manufacturing chamber between carbon atoms vaporized from the melt pool during laser exposure and the nitrogen atmosphere. The laser beam performs a dual action: it splits the nitrogen molecule (N_2) into atomic nitrogen (N) and vaporizes the carbon atoms. The C_3N_4 formed in atmosphere falls to the residual powder during the layer-by-layer manufacturing process. To confirm the formation of C_3N_4 in atmosphere and to understand the mechanisms involved, the powder collected by the cyclone filter, here called "black powder", was analyzed. The black powder contains the

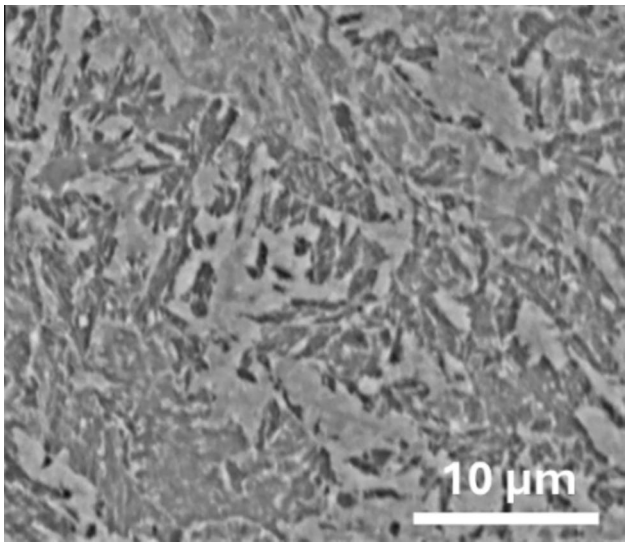

Fig. 3 SEM image of the P210v100 sample microstructure after chemical etching with 2% Nital

Table 4 Surface energy density (SED) and average value of relative mass density (ρ) of AISI 1070 samples manufactured by L-PBF

Sample designation	SED (J/mm^2)	ρ (%)
P190v150	9.0	98.9
P210v100	15.0	98.9
P210v150	10.0	98.6
P210v200	7.5	97.8

Table 5 Chemical composition by mass % in the center of the P210v100 sample. The second row shows the results obtained with EDS, which agree with the OES results

	C	Si	Mn	P	S	Cr	Mo	V	Ni
OES	0.55	0.18	0.52	0.011	0.006	0.40	0.06	0.05	0.45
EDS		0.2	0.52	0.01	0.01				

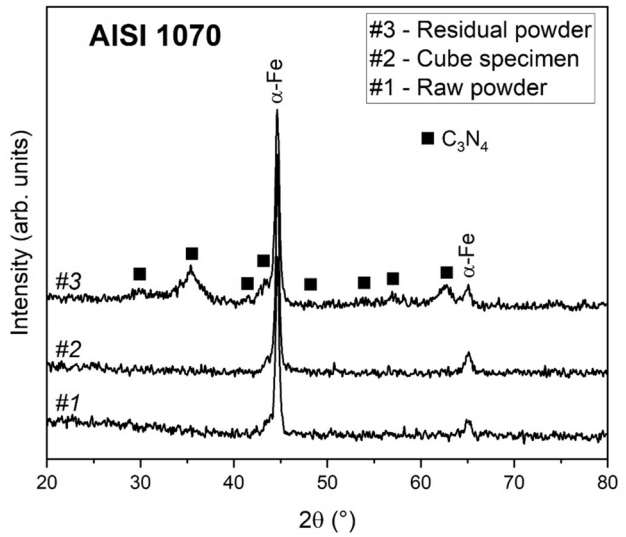

Fig. 4 XRD patterns of the samples: #1—raw powder, #2—cube P210v100 specimen and #3—residual powder in the chamber after fabrication. The diffraction peaks of the α-Fe phase are labeled, while those of C_3N_4 marked by solid squares. The patterns are shifted vertically for better comparison

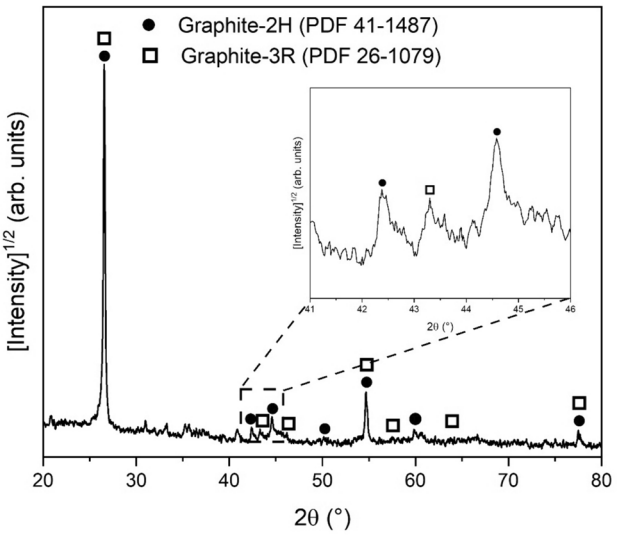

Fig. 5 XRD pattern of pure graphite rod ground to powder. The inset shows diffraction peaks in the angular range $2\theta = 41°–46°$

waste material produced in the production chamber and is blown by the flowing nitrogen. The presence of C_3N_4 in the black powder suggests that the C–N reaction preferentially occurs in the atmosphere rather than on the surface of the sample, during or after the laser exposure. After formation, C_3N_4 is collected in the filtering system. The fact that XRD pattern #3 in Fig. 4 shows broad and low intensity C_3N_4 peaks means that the compound is poorly crystallized, which is consistent with the conjectured reaction in the atmosphere.

3.2 *Reactive formation of C_3N_4 in N_2 atmosphere by sublimation of a pure graphite rod with high values of SED*

To study the presence of C_3N_4 in the black powder, a rod of pure graphite was exposed to the laser beam to cause the sublimation of the graphite and thus the reaction of the carbon atoms with the nitrogen atmosphere. The pure graphite rod was ground in a mortar to a polycrystalline powder in order to carry out a structural characterization by XRD and FTIR. Results of the XRD investigation of the pulverized graphite rod are shown in Fig. 5.

The XRD pattern in Fig. 5 is given in square root intensity to emphasize the lower intensity peaks and shows that the powder consists of two different types of C–graphite, namely: (a) C—Graphite-2H, hexagonal, space group P63/mmc (194), lattice parameters $a = 0.24704$ nm and $c = 0.67244$ nm (ICDD-PDF file no. 41–1487) and (b) C—Graphite-3R, RhomboH axes, space group R3 (146), lattice parameters $a = 0.2456$ and $c = 1.0044$ nm (ICCD-PDF file no. 26–1079). Inset in Fig. 5 is an enlargement of the area marked by the dashed rectangle in the XRD pattern, which shows the diffraction peaks of the two graphite phases in the short angular range $2\theta = 41°–46°$. The FTIR spectrum of the pulverized graphite rod (not shown here) demonstrates the presence of organic material such as aliphatic hydrocarbons, which are used as binders for graphite [26, 27].

The graphite rod was exposed to the laser beam using the combination of process parameters reported in Table 6, where both short and long samples names are indicated. The sublimation of the rod graphite was achieved by multiple scans without hatching space.

In order to obtain high SED values up to 7143 J/mm^2, the laser beam was operated at $P = 900$ W with different scanning speeds (Table 6). The high laser power is needed to achieve the vaporization of the carbon atoms from the rod and the dissociation of the nitrogen molecules (N_2) in the atmosphere into atomic nitrogen (N) ready to react with the carbon atoms. In principle, this should increase the total amount of C_3N_4 formed in the atmosphere and thus the amount of C_3N_4 collected in the cyclone filter. The results of the structural characterization by XRD and FTIR of the black powder collected in the cyclone filter after laser-induced sublimation of the graphite rod are shown in Fig. 6. The XRD patterns (Fig. 6A) are given in square root intensity in the angular range $2\theta = 41°–46°$ to better distinguish the diffraction peaks of graphite and C_3N_4.

It is worth noting that the shape and position of the peaks in the range $2\theta = 42–44°$ in Fig. 6A, which include the C-2H (100), C_3N_4 (210) and C-3R (101) diffraction peaks, depend strongly on the SED, while the C-2H (101) peak remains almost unaltered. At the highest SED value (7143 J/

Table 6 Process parameters used to sublimate the graphite rod by the laser beam

Short sample name	Long sample name	*P* (W)	*V* (mm/s)	*H* (mm)	SED (J/mm^2)
#900/1	P900V0.9	900	0.9	0.14	7143
#900/2	P900V1.8		1.8		3571
#900/3	P900V3.4		3.4		1891

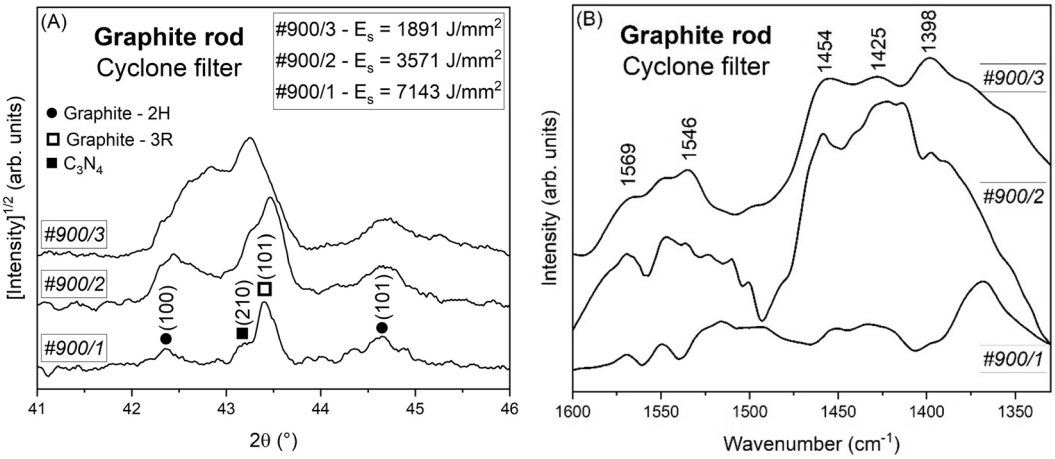

Fig. 6 Black powder collected in the cyclone filter after laser sublimation of the graphite rod at $P = 900$ W: **A** XRD patterns, **B** FTIR spectra. The XRD patterns are shown in square root intensity in the short angular range $2\theta = 41°–46°$. Full dot—Graphite-2H, open square—Graphite-3R, full square—C_3N_4. Numbers are Miller indexes of the XRD reflection. In both figures, the patterns are shifted vertically for better comparability

mm^2, pattern #900/1 in Fig. 6A), the peaks are well separated, although the C_3N_4 (210) reflection is quite low. At SED = 3571 J/mm^2 (pattern #900/2 in Fig. 6A), the C_3N_4 (210) and C-3R (101) peaks tend to shift to higher angles, as a consequence of the smaller lattice parameters of the compounds. On the other hand, analyzing the peak shape showed that the C_3N_4 (210) peak increases in intensity, suggesting higher amount of C_3N_4 collected in the cyclone filter. At the lowest value of SED (1891 J/mm^2, pattern #900/3 in Fig. 6A), the three peaks tend to overlap, resulting in a broad diffraction effect that can be deconvoluted by peak shape analysis. In this case, both C_3N_4 and C-3R increase their lattice parameters (diffraction peaks shifted to lower angles), while the C_3N_4 (210) peak shows its highest intensity compared to all other samples, suggesting massive formation of C_3N_4 at the lowest SED value. This is confirmed by the FTIR analysis. Figure 6B depicts the FTIR spectra of the black powder collected in the cyclone filter. The spectra of samples #900/2 and #900/3 exhibit a similar trend, confirming the presence of triazine units organized in the C_3N_4 compound. The adsorption peaks within the 1300–1600 cm^{-1} range can be attributed to C–N and C=N stretching vibrations of the aromatic CN repeating unit [28]. Characteristic out-of-plane vibrations of triazine units are confirmed by peaks at 859 and 806 cm^{-1} (not shown here) [29]. In the spectrum of sample #900/1, the characteristic bands of C_3N_4 display lower peak intensities, indicating a lower concentration of carbon nitride. On the contrary, in the spectrum #900/3, the peaks associated with C_3N_4 are well defined with high intensity (Fig. 6B), indicating a massive formation of this compound. The characteristic peaks of the hydrocarbon portion (not shown here) can also be recognized in the FTIR spectra, suggesting contamination by additives or paraffinic material in the chamber.

Divergent spectral trends among the samples highlight that, as reported in the literature [14], C_3N_4 is composed of rigid planes of triazine units formed in a temperature range between 550 and 700 °C. Different values of these parameters can destabilize the rigid plane of the structure, which disintegrates into smaller fragments such as nanosheets.

3.3 *Reactive formation of C_3N_4 in N_2 atmosphere as a by-product of the AISI 1070 parts produced with high values of SED*

Following the results obtained with the graphite rod, the same laser parameters reported in Table 6 were adopted to produce $12 \times 12 \times 12$ mm^3 cube specimens of AISI 1070, in order to study the formation of C_3N_4 as a by-product of manufacturing. Also in this case, the black powder collected in the cyclone filter was analyzed by XRD and FTIR. The

results are shown in Fig. 7 for the specimen built with the lowest SED value of 1891 J/mm^2.

The XRD pattern in Fig. 7A shows the α-Fe (110) diffraction peak of the body centered cubic ferritic phase and a broad and low intensity peak of C_3N_4, which indicates low crystallinity of C_3N_4. Figure 7B shows the FTIR spectrum of AISI 1070 black powder collected from the cyclone filter. The spectral pattern strongly suggests the presence of the C_3N_4 material, characterized by bands at 1626 cm^{-1} (C=N bond), 1489 cm^{-1}, and 1401 cm^{-1} (C–N bond). The high intensity peak at 3423 cm^{-1} was attributed to the stretching vibrations of non-condensed primary (–NH–) and secondary ($–NH_2$) amines present in the residual amino groups at the edges of the aromatic ring of the triazine units. The presence of metal atoms and other impurities originating from the laser melting of the AISI 1070 raw powder likely influences the formation of C_3N_4 as it forms coordination bonds with the triazine units and keeps them separated from each other. Overall, however, the formed carbon nitride appears to be homogeneous, with no evidence of hydrocarbon contamination.

Metal atoms have a significant effect on the structure and properties of carbon nitrides. Alwin et al. [30] demonstrated that metal doping at the molecular level can regulate the structure of carbon nitride materials and lead to enhanced catalytic activity. Furthermore, the introduction of metals onto the surface of carbon nitride can result in changes such as an increase in the specific surface area, atomic ratio, and number of defects in the crystalline structure [31]. The coordination of metal complex fragments to carbon nitride can also tune its properties and lead to the development of novel catalysts. Chen et al. [32] showed that various carbon nitride scaffolds, such as linear melem oligomers and poly(triazine/heptazine imides), can effectively isolate metal atoms and influence their average oxidation state. Overall, the presence of metal atoms in carbon nitrides can enhance their photocatalytic, electrocatalytic, and catalytic activities, opening up new avenues for various applications [33].

4 Conclusions

In this experimental work, the findings from three key experiments were presented: (1) Successful manufacturing of AISI 1070 steel parts by L-PBF in nitrogen atmosphere (SED = 0.67–15 J/mm^2), and the simultaneous reactive formation of C_3N_4 as a by-product; (2) Laser sublimation of a pure graphite rod in nitrogen atmosphere (SED = 1891–7143 J/mm^2) to enhance the production of the C_3N_4 compound; and (3) Manufacturing of parts in AISI 1070 in a nitrogen atmosphere at high values of surface energy density (SED = 1891–7143 J/mm^2), for improving the production of the C_3N_4 material.

The results obtained can be summarized as follows:

- AISI 1070 parts with a density of over 98% were successfully manufactured with a laser power of 210 W and a SED value of 15 J/mm^2. The microstructure and composition of the components align closely with standard specifications and are suitable for various industrial applications;
- C_3N_4 (ICDD-PDF file no. 53-0671) with hexagonal lattice structure was detected in the residual powder as a result of the reaction between the nitrogen atmosphere and the carbon atoms vaporized during the laser beam exposure;
- XRD and FTIR analyses confirmed the presence of C_3N_4 in the black powder collected from the cyclone filter after

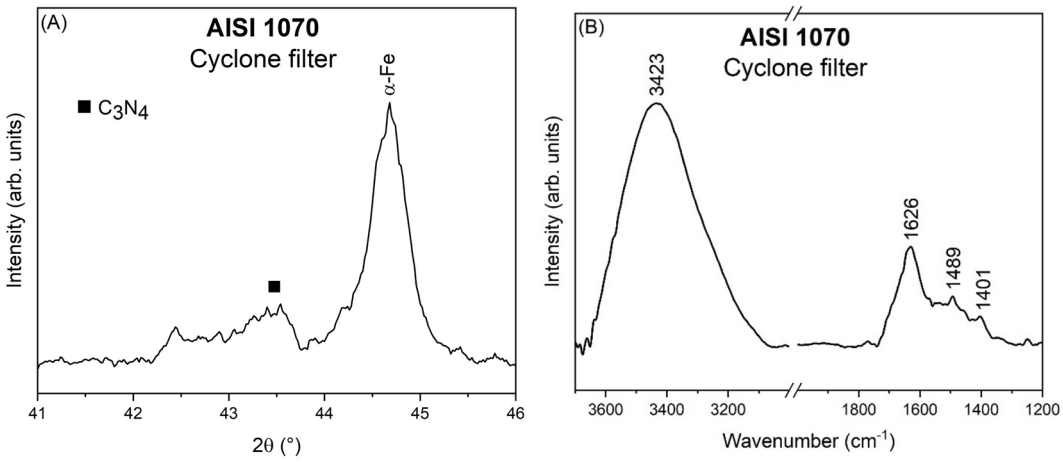

Fig. 7 Black powder collected in the cyclone filter during the production of AISI 1070 specimens at $P = 900$ W: **A** XRD pattern in the reduced angular range $2\theta = 41°–46°$, full square—C_3N_4 and **B** FTIR spectrum in the wavenumber range 3700–1200 cm^{-1}

sublimation of a pure graphite rod at SED values of up to 7143 J/mm^2;

- The black powder collected from the cyclone filter after the manufacturing of AISI 1070 parts with high SED values contains C_3N_4 with a high amount of residual amino groups located at the edges of the aromatic ring of the triazine units. This effect is due to the vaporization of metal atoms and impurities from the melt pool, which interfere with the formation mechanism of C_3N_4.

In conclusion, this study underscores the innovative accomplishment of synthesizing carbon nitride as a valuable by-product during the production of functional AISI 1070 steel parts via L-PBF, achieved through reaction with a nitrogen atmosphere. Therefore, the technology of reactive laser powder bed fusion, based on the laser-induced reaction between vaporized atomic species and the atmosphere, opens up new perspectives for numerous scientific and industrial applications.

Acknowledgements The authors would like to acknowledge the support received from the technicians of 3D4MEC SrL, Sasso Marconi (BO), Italy.

Funding Open access funding provided by Università Politecnica delle Marche within the CRUI-CARE Agreement.

Data availability Data available on request from the authors.

Declarations

Conflict of interest The authors declare that they have no known competing financial interests or personal relationships that could have appeared to influence the work reported in this paper.

References

1. Goetz IK, Kaplan M, Hans M, Ström P, Jansson U, Hjörvarsson B, Schneider JM (2023) Reactive metal additive manufacturing: surface near ZrN–metallic glass composite formation and mechanical properties. Addit Manuf 66:103457. https://doi.org/10.1016/j.addma.2023.103457
2. Sahasrabudhe H, Bandyopadhyay A (2018) In situ reactive multi-material Ti6Al4V-calcium phosphate-nitride coatings for bio-tribological applications. J Mech Behav Biomed Mater 85:1–11. https://doi.org/10.1016/j.jmbbm.2018.05.02
3. Dong Y, Wang D, Li Q, Luo X, Zhang J, Prashanth KG, Yan M (2023) Strong and ductile titanium via additive manufacturing under a reactive atmosphere. Mater Today Adv 17:100347. https://doi.org/10.1016/j.mtadv.2023.100347
4. Peters AB, Zhang D, Hernandez A, Brupbacher MC, Nagle DC, Mueller T, Spicer JB (2021) Selective laser sintering in reactive atmospheres: Towards in-situ synthesis of net-shaped carbide and nitride ceramics. Addit Manuf 45:102052. https://doi.org/10.1016/j.addma.2021.102052
5. Peters AB, Wang C, Zhang D, Hernandez A, Nagle DC, Mueller T, Spicer JB (2023) Reactive laser synthesis of ultra-high-temperature ceramics HfC, ZrC, TiC, HfN, ZrN, and TiN for additive manufacturing. Ceram Int 49(7):11204–11229. https://doi.org/10.1016/j.ceramint.2022.11.319
6. Haines MP, Peter NJ, Babu SS, Jägle EA (2020) In-situ synthesis of oxides by reactive process atmospheres during L-PBF of stainless steel. Addit Manuf 33:101178. https://doi.org/10.1016/j.addma.2020.101178
7. Wang Y, Wang B, Luo L, Oliveira JP, Li B, Yan H, Chen D (2023) Effects of process atmosphere on additively manufactured FeCrAl oxide dispersion strengthened steel: Printability, microstructure and tensile properties. Mater Sci Eng A 882:145438. https://doi.org/10.1016/j.msea.2023.145438
8. Yin H, Wei B, Shmatok A, Yang J, Salek MF, Beckingham L, Lou X (2023) On the nanoscale oxide dispersion via in-situ atmospheric oxidation during laser powder bed fusion. J Mater Process Technol 322:118191. https://doi.org/10.1016/j.jmatprotec.2023.118191
9. Horn T, Rock C, Kaoumi D, Anderson I, White E, Prost T, Darsell J (2022) Laser powder bed fusion additive manufacturing of oxide dispersion strengthened steel using gas atomized reaction synthesis powder. Mater Design 216:110574. https://doi.org/10.1016/j.matdes.2022.110574
10. Chen M, Zhang H, Li H, Zhao Z, Wang K, Zhou Y, Dubal DP (2024) CxNy-based materials as gas sensors: structure, performance, mechanism and perspective. Coordinat Chem Rev 503:215653. https://doi.org/10.1016/j.ccr.2023.215653
11. Liebig JV (1834) About some nitrogen compounds. Ann Pharm 10(10):10
12. Wang X, Maeda K, Thomas A, Takanabe K, Xin G, Carlsson JM, Antonietti M (2009) A metal-free polymeric photocatalyst for hydrogen production from water under visible light. Nat Mater 8(1):76–80. https://doi.org/10.1038/nmat2317
13. Priyanga GS, Pransu G, Sampath S (2023) A comprehensive overview of the graphitic-carbon nitride computational approach: from basic properties to a wide range of applications. Chem Phys Impact. https://doi.org/10.1016/j.chphi.2023.100408
14. Praus P, Svoboda L, Ritz M, Troppová I, Šihor M, Kočí K (2017) Graphitic carbon nitride: synthesis, characterization and photocatalytic decomposition of nitrous oxide. Mater Chem Phys 193:438–446. https://doi.org/10.1016/j.matchemphys.2017.03.008
15. Qureshi WA, Haider SNUZ, Naveed A, Ali A, Liu Q, Yang J (2023) Recent progress in the synthesis, characterization and photocatalytic application of energy conversion over single metal atoms decorated graphitic carbon nitride. Int J Hydrogen Energy. https://doi.org/10.1016/j.ijhydene.2022.11.181
16. Deifallah M, McMillan PF, Corà F (2008) Electronic and structural properties of two-dimensional carbon nitride graphenes. J Phys Chem C 112(14):5447–5453. https://doi.org/10.1021/jp711483t
17. Qamar MA, Javed M, Shahid S, Shariq M, Fadhali MM, Ali SK, Khan MS (2023) Synthesis and applications of graphitic carbon nitride (g-C_3N_4) based membranes for wastewater treatment: A critical review. Heliyon. https://doi.org/10.1016/j.heliyon.2022.e12685

18. Anus A, Park S (2024) The synthesis and key features of 3D carbon nitrides (C3N4) used for CO_2 photoreduction. Chem Eng J. https://doi.org/10.1016/j.cej.2024.150213
19. López-Salas N, Albero J (2021) CxNy: new carbon nitride organic photocatalysts. Front Mater 8:772200. https://doi.org/10.3389/fmats.2021.772200
20. Li G, Li X, Guo C, Zhou Y, Tan Q, Qu W, Li X, Hu X, Zhang M-X, Zhu Q (2022) Investigation into the effect of energy density on densification, surface roughness and loss of alloying elements of 7075 aluminium alloy processed by laser powder bed fusion. Opt Laser Technol 147:107621. https://doi.org/10.1016/j.optlastec.2021.107621
21. Gatto A, Gatto ML, Groppo R, Munteanu D, Mengucci P (2023) Influence of laser powder bed fusion process parameters on the properties of CuZn42 components: case study of the laser surface energy density. Prog Addit Manufact 8(5):843–855. https://doi.org/10.1007/s40964-022-00361-z
22. Gordon JV, Narra SP, Cunningham RW, Liu H, Chen H, Suter RM, Beuth JL, Rollett AD (2020) Defect structure process maps for laser powder bed fusion additive manufacturing. Addit Manuf 36:101552. https://doi.org/10.1016/j.addma.2020.101552
23. Nakamoto T, Shirakawa N, Miyata Y, Inui H (2009) Selective laser sintering of high carbon steel powders studied as a function of carbon content. J Mater Process Technol 209(15–16):5653–5660. https://doi.org/10.1016/j.jmatprotec.2009.05.022
24. Yue T, Zou Z, Zhang S, Xu Y, Zang Y (2023) Influence of volumetric energy density on the tribological behaviors of pure nickel fabricated by laser powder bed fusion. Virtual Phys Prototyp 18(1):e2262449. https://doi.org/10.1080/17452759.2023.2262449
25. Viafara CC, Castro MI, Vélez JM, Toro A (2005) Unlubricated sliding wear of pearlitic and bainitic steels. Wear 259(1–6):405–411. https://doi.org/10.1016/j.wear.2005.02.013
26. Liu J, Zhang T, Wang Z, Dawson G, Chen W (2011) Simple pyrolysis of urea into graphitic carbon nitride with recyclable adsorption and photocatalytic activity. J Mater Chem 21(38):14398–14401. https://doi.org/10.1039/C1JM12620B
27. Mohini R, Lakshminarasimhan NJMRB (2016) Coupled semiconductor nanocomposite g-C_3N_4/TiO_2 with enhanced visible light photocatalytic activity. Mater Res Bull 76:370–375. https://doi.org/10.1016/j.materresbull.2015.12.034
28. Chang F, Zhang J, Xie Y, Chen J, Li C, Wang J, Hu X (2014) Fabrication, characterization, and photocatalytic performance of exfoliated g-C_3N_4–TiO_2 hybrids. Appl Surf Sci 311:574–581. https://doi.org/10.1016/j.apsusc.2014.05.111
29. Bledowski M, Wang L, Ramakrishnan A, Khavryuchenko OV, Khavryuchenko VD, Ricci PC, Beranek R (2011) Visible-light photocurrent response of TiO_2–polyheptazine hybrids: evidence for interfacial charge-transfer absorption. Phys Chem Chem Phys 13(48):21511–21519. https://doi.org/10.1039/C1CP22861G
30. Alwin E, Wojcieszak R, Kočí K, Edelmannová M, Zieliński M, Suchora A, Pietrowski M (2022) Reductive modification of carbon nitride structure by metals—the influence on structure and photocatalytic hydrogen evolution. Materials 15(3):710. https://doi.org/10.3390/ma15030710
31. Bai Y, Zheng Y, Wang Z, Hong Q, Liu S, Shen Y, Zhang Y (2021) Metal-doped carbon nitrides: synthesis, structure and applications. New J Chem 45(27):11876–11892. https://doi.org/10.1039/D1NJ02148F
32. Chen Z, Vorobyeva E, Mitchell S, Fako E, López N, Collins SM, Pérez-Ramírez J (2018) Single-atom heterogeneous catalysts based on distinct carbon nitride scaffolds. Natl Sci Rev 5(5):642–652. https://doi.org/10.1093/nsr/nwy048
33. Rudenkov AS, Piliptsou DG, Rogachev AV, Fedosenko NN, Jiang X (2017) Impact of ion nitriding on phase composition, structure and properties of carbon films doped with metals. In: Recent Global Research and Education: Technological Challenges: Proceedings of the 15th International Conference on Global Research and Education Inter-Academia 2016 (pp. 11–18). Springer International Publishing. https://doi.org/10.1007/978-3-319-46490-9_2